

# Contrast-enhanced robotic capsule tracking in ultrasound using a dynamic acoustic retroreflector

Ann Ping<sup>1</sup>, Giovanni Faoro<sup>2</sup>, Veronica Iacovacci<sup>2</sup>, Arianna Menciassi<sup>2</sup>, and Eric Diller<sup>1</sup>

**Abstract**—Ingestible robotic capsules are a minimally-invasive option for diagnosing and treating conditions of the gastrointestinal tract. Ultrasound has the potential to provide the accurate and real-time image guidance that is necessary for site-specific procedures; however, existing ultrasound-based methods have limited clinical utility due to factors such as low capsule contrast, high background noise, unsuitable capsule motion requirements, low frame rates, and reliance on raw ultrasound radiofrequency data, which is rarely accessible in clinical systems. This work presents a high-contrast ultrasound tracking target that can be equipped on a robotic capsule, and that emits a periodic flashing signal in clinically-available B-mode images. The tracking target is a shape-changing acoustic retroreflector whose retroreflection can be constructed and destroyed by changing the device's configuration under magnetic actuation. Subsequent spatial localization of the periodic intensity signal in B-mode is accomplished with an efficient Fourier-based network. Tracking of a stationary mock capsule was evaluated in an *ex-vivo* porcine stomach-agar phantom using a stationary and moving ultrasound probe. The mean tracking error was 2.2 mm with a stationary probe and 3.0 mm with a moving probe. Tracking update rates reached up to 120 Hz. Our method is compatible with B-mode, stationary capsules, and a moving probe, demonstrating potential for clinical use in the localization of robotic capsules.

## I. INTRODUCTION

Ingestible robotic capsules aid the diagnosis and treatment of the gastrointestinal tract through tasks such as endoscopy, microbiome sampling, tissue biopsy, and drug delivery. These robotic capsules typically traverse through the gut passively until they reach a target site. To achieve external guidance and locomotion for site-specific procedures, not only is the accurate and real-time tracking of the capsule position necessary, but also the concurrent imaging of physiological tissue to provide reference for the gastrointestinal environment. Magnetic resonance imaging (MRI) and X-ray can image tissue, but MRI has low temporal resolution and cannot safely image magnetic capsules in the body, and X-ray deposits harmful ionizing radiation. Ultrasound imaging offers a promising solution for the image-guidance of

gastrointestinal capsules because it is non-invasive, portable, inexpensive, has good temporal and spatial resolution, and can image deep tissue structures. However, a significant challenge in ultrasound-based robotic capsule tracking is that typical capsule materials (e.g., rubber, plastic) do not offer high contrast against physiological tissue in Brightness (B)-mode ultrasound. Additionally, intraluminal gas can produce artifacts in the ultrasound image that obscure the capsule [1]. Motion-based tracking can overcome contrast challenges inherent to tracking based on static image segmentation. In motion-based tracking, the robot undergoes a known motion pattern; this motion against a static background can be used as contrast for improved detection.

The current state-of-the-art motion-based tracking methods for microrobots in ultrasound are color Doppler, ultrasound acoustic phase analysis (US-APA), and ultrasound optical flow (US-OF). Color Doppler is a traditional technique that detects flow velocity based on phase shifts in the raw ultrasound radiofrequency (RF) signal. Color Doppler has high frame rates (30 Hz), and has successfully tracked moving microswarms in vascular phantoms [2], but suffers from noise caused by counter flow and tissue motion [3]. US-APA is a novel technique that uses Fourier analysis to track the location of RF phase shifts produced by a moving microrobot [3]–[6]. US-APA is robust and more sensitive to characteristic microrobot motion patterns than Doppler, but is still limited in its clinical feasibility due to low frame rates (1–2 Hz) and its reliance on RF data. In contrast, US-OF is a computer vision-based approach that computes velocity maps of B-mode images, and detects a moving microrobot by searching for regions of high velocity [7]. US-OF has high frame rates (40 Hz) and can be performed on clinically available B-mode data; however, it is sensitive to any motion in the field of view. This is unfavorable in a clinical setting because the ultrasound probe must move during an abdominal scan, yet US-OF velocity maps produce significant noise at tissue regions when imaged by a moving probe due to the relative motion of B-mode speckle. Furthermore, color Doppler, US-APA, and US-OF are dependent on the bulk motion of the robot for detection. In cases where a robotic capsule must be stationary, such as to carefully excise tissue during biopsy, it is unsuitable to impose bulk motion on the capsule simply to localize it. Finally, unlike the bulk motion of a micro-scale robot, that of a larger capsule will cause adjacent gastrointestinal lumen tissue to move in a similar motion pattern, producing noise. Therefore, there is a need for an alternative robotic capsule motion-based tracking method in ultrasound that is more clinically feasible than

\*We acknowledge the support of the Natural Sciences and Engineering Research Council of Canada (NSERC) and the Ontario Graduate Scholarship

<sup>1</sup>Ann Ping and Eric Diller are with the Department of Mechanical and Industrial Engineering, University of Toronto, 5 King's College Rd, Toronto, ON M5S 3G8, Canada ann.ping@mail.utoronto.ca, ediller@mie.utoronto.ca

<sup>2</sup>Giovanni Faoro, Veronica Iacovacci, and Arianna Menciassi are with The BioRobotics Institute & Department of Excellence in Robotics & AI, Scuola Superiore Sant'Anna, 56127 Pisa, Italy giovanni.faoro@santannapisa.it, veronica.iacovacci@santannapisa.it, arianna.menciassi@santannapisa.it

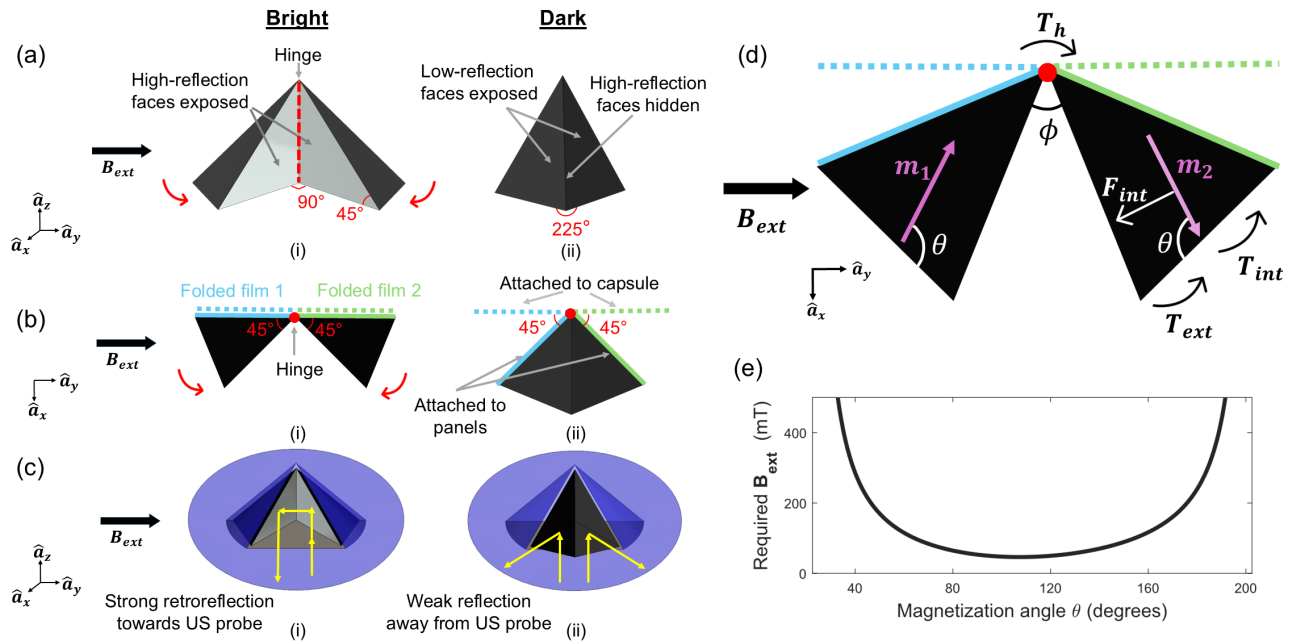


Fig. 1. Structural design and magnetic actuation of the dynamic CCR. (a) Front view of the dynamic CCR. (i) Bright configuration: reflective faces of the tetrahedral panels are orthogonal and face the ultrasound probe. (ii) Dark configuration: low-reflection faces are exposed and angled away from the probe. (b) Hinge design in top view. The hinge is formed using two separate sheets of folded thin film (blue and green). Dashed lines: the half of film that is connected to the capsule cavity inner wall. Solid lines: the half that is connected to the adjacent panel face. (i) Bright configuration. (ii) Dark configuration. (c) Integration of dynamic CCR with capsule (shown as translucent blue) (i) in the cavity in the bright configuration to form a complete 3D CCR, and (ii) in the cavity in the dark configuration. (d) Schematic of applied torques and forces on the right-side panel as a free-body diagram. Magnetic moments (in purple) are angled at  $\theta$ , and the panel opening angle is  $\phi$ . (e) Calculated required external magnetic field to achieve bright configuration for different  $\theta$ .

existing methods. Specifically, a clinically useful tracking method would possess four qualities: B-mode compatibility, high sensitivity to the robot position even during probe motion, high frame rates, and independence from capsule bulk motion.

Our work addresses all four clinical requirements using a novel approach where the capsule emits a periodic flashing signal in B-mode, which behaves as a high contrast tracking target. We introduce a moving dynamic acoustic retroreflector that can be functionalized onto the surface of a robotic capsule. Through the magnetically actuated opening and closing of the retroreflector, periodic intensity changes are induced in the B-mode images. The location of the periodic intensity pattern is tracked using a computationally efficient Fourier technique, providing the real-time location of the device.

## II. DESIGN AND ACTUATION MECHANISM

This section addresses the design considerations for the dynamic acoustic retroreflector, including structural and material considerations for maximizing the contrast of the device in ultrasound B-mode, and magnetic actuation considerations for minimizing the required magnetic field strength to initiate the flashing pattern.

### A. Structural and Material Design

The following subsections describe how the geometry and acoustic impedance of the device were designed to maximize its brightness and darkness in ultrasound, to consequently enhance the visibility of the flashing pattern.

1) *Geometry*: An acoustic retroreflector reflects sound waves back to their source regardless of incident angle. Because the ultrasound probe is both the source and detector of acoustic waves, a retroreflector would direct incident waves back to the probe with minimal scattering or specular reflection away from the probe. A corner cube retroreflector (CCR) consists of three flat, intersecting, and orthogonal faces. The dynamic CCR presented in this work is based on the opening and closing of an acoustic CCR to produce a strong periodic flashing in ultrasound B-mode. The structural design is shown in Figure 1(a), (b), and (c). The dynamic CCR consists of two congruent tetrahedral panels situated within a cavity in the capsule shell, and connected to one another and to the cavity's inner wall by a hinge. The bottom surface of the cavity and the two inner faces of the panels are acoustically reflective. In the bright configuration, all three reflective faces are mutually orthogonal, constructing the CCR. In the dark configuration, the reflective faces are hidden, and the low-reflection faces of the two panels are exposed to the probe at a reflex angle to direct reflected rays away from the probe, producing a dark area in the ultrasound image. The hinge allows for the 45° rotation of both panels between the bright and dark configurations. The hinge is formed by folding two thin triangular films in half and adhering one half of each film to the surface of the panel facing the cavity and the other half to the inner wall of the cavity itself.

2) *Acoustic Impedance*: The greater the relative difference between the acoustic impedance of a material and

its surrounding physiological environment, the greater the amplitude of reflected acoustic waves at the material-tissue interface, and the brighter the material appears in ultrasound. Metals have high impedance ( $>15$  MRayl), which is why aluminum film was selected as the reflective surface in this device. In contrast, silicone rubber has an impedance (1.1 MRayl) closer to that of tissue (1.4–1.7 MRayl) [8], making it suitable as the low-reflection material.

### B. Magnetic Actuation

The tetrahedral panels are composed of a magnetorheological elastomer formed by embedding neodymium-iron-boron (NdFeB) nanoparticles in silicone rubber. The panels act as bonded magnets which can be approximated by dipole magnetic moments of  $\mathbf{m}_1$  and  $\mathbf{m}_2$ . The summation of the panel moments produces a net magnetic moment to the dynamic CCR. The dynamic CCR is normally in the dark configuration until an external magnetic field ( $\mathbf{B}_{\text{ext}}$ ) is applied. The field produces a torque ( $\mathbf{T}_{\text{ext}}$ ) on each moment, which rotates the panels away from one another about the hinge at angle  $\phi$ , bringing about the bright configuration. Each panel also experiences a torque ( $\mathbf{T}_{\text{int}}$ ) and force ( $\mathbf{F}_{\text{int}}$ ) from the other, as well as a torque from the hinge ( $\mathbf{T}_h$ ). The forces and torques on the CCR panels are illustrated in Figure 1(d).

The optimal magnetization angle  $\theta_0$  balances minimum attraction force  $\mathbf{F}_{\text{int}}$  between the magnets with maximum  $\mathbf{T}_{\text{ext}}$ . To determine  $\theta_0$ , the  $\theta$  at the minimum of  $B_{\text{ext}}(\theta)_y$  was determined.  $B_{\text{ext}}(\theta)_y$  is the y-component of the required external magnetic field to achieve the bright configuration (i.e., to overcome the internal forces between the magnets in the dark configuration).  $B_{\text{ext}}(\theta)_y$  was calculated for  $22.5^\circ < \theta < 202.5^\circ$  according to

$$B_{\text{ext}}(\theta)_y = \frac{\|\mathbf{T}_{\text{int}}(\theta) + \mathbf{L} \times \mathbf{F}_{\text{int}}(\theta)\|}{m \sin(\theta - 22.5^\circ)}, \quad (1)$$

where  $\mathbf{L}$  is the position vector from the hinge center to the magnet's centroid and  $\theta - 22.5^\circ$  is the angle between  $\mathbf{B}_{\text{ext}}$  and  $\mathbf{m}_2$ .  $\mathbf{T}_h$  was assumed negligible due to the compliance of the thin hinge material.  $m = m_1 = m_2$  was measured experimentally to be  $5.94 \times 10^{-4}$  Am<sup>2</sup> for a 60% w/w concentration of NdFeB using anisotropic magneto-resistive sensors (m-axis, matesy GmbH). The theoretical required magnetic field as a function of  $\theta$  is shown in Figure 1(e). The minimum required field was calculated to be 46.3 mT at an angle of  $\theta = \theta_0 = 107.3^\circ$ .

## III. EXPERIMENTAL SET-UP

This section details the fabrication of the dynamic CCR and the ultrasound phantom, as well as the B-mode image collection and analysis procedure.

### A. Fabrication

The panels of the dynamic CCR were formed in a mold containing a mixture of 60% w/w NdFeB nanoparticles (MQFP-15-7, Neo Magnequench) and silicone rubber (Mold Star 30, Smooth-On, Inc.). After curing, the panels were

removed and magnetized at  $107.3^\circ$  in a strong uniform magnetic field (3.0 T) generated by an impulse magnetizer (9 Tesla Pulse Magnetiser, Magnetic Measurements Ltd.). A mock capsule was molded using silicone rubber, and aluminized polyethylene terephthalate (polyester; PET) film (thickness=51  $\mu\text{m}$ ) was adhered to the bottom surface of the capsule cavity. Aluminized PET film was also adhered to the inner faces of the panels, and clear PET film (thickness=13  $\mu\text{m}$ ) was folded in half and adhered to the posterior panel faces and the capsule cavity to form the hinge. Figure 2(a) shows an image of the dynamic CCR integrated with a mock capsule.

### B. Ultrasound Compatible Phantom

An agar phantom ( $10 \times 10 \times 10$  cm) was used to simulate the gastrointestinal environment. The phantom contained a channel ( $6 \times 3 \times 4$  cm,  $L \times W \times H$ ) that was lined with porcine stomach tissue and filled with water to mimic the gut lumen. To mimic the acoustic properties of physiological tissue, the phantom was composed of distilled water, agar (3% w/v), glycerol (8% v/v), and cellulose scattering particles (1.5% w/v) [9].

### C. Image Collection

Figure 2(b) depicts the imaging of the dynamic CCR. The mock capsule, with the dynamic CCR in a cavity, was placed in the channel of the phantom facing a linear ultrasound probe (L15-7H40, Teleded, Lithuania). The mock capsule was kept stationary during imaging. The dynamic CCR was imaged in B-mode with a research ultrasound system (Teleded ArtUs EXT-1H; frequency = 7.5 MHz; wideview mode; depth = 8 cm).

A cubic permanent magnet (2.54 cm) was manually brought towards and away from the phantom along the y-axis to apply and remove the magnetic field, respectively, at an approximate frequency of 2 Hz. Magnet movement was manual to demonstrate that tracking could be successful without precisely controlling the oscillation frequency and field strength. During field application, the distance between

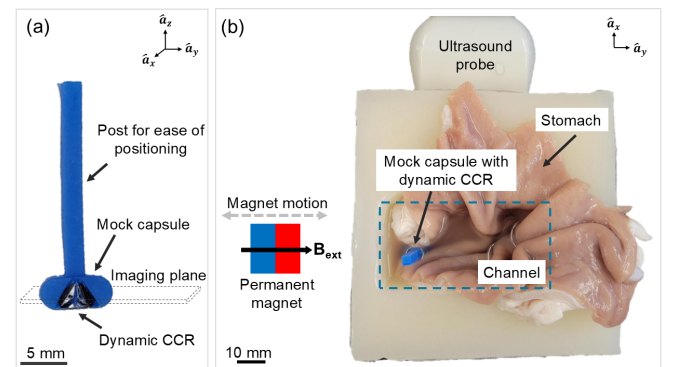


Fig. 2. (a) Image of the dynamic CCR in a cavity in a mock capsule. The mock capsule was attached to a post for ease of positioning. The dynamic CCR intersects the imaging plane (x-y plane). (b) Experimental platform depicting the dynamic CCR integrated with a mock capsule, the agar-stomach phantom, the ultrasound probe, and a permanent magnet.

the center of the magnet and the dynamic CCR was between 4.5–5.5 cm, corresponding to fields between 25–46 mT.

B-mode images were collected of a stationary mock capsule under two probe motion schemes: stationary and moving within the imaging plane.

The ultrasound probe was attached to a 7-DOF robotic arm (Franka Emika) to achieve smooth motion within the imaging plane with a linear speed up to 4.5 mm/s. Five trials per motion scheme were conducted to demonstrate repeatability, with the mock capsule re-positioned between trials.

#### D. Motion Analysis

B-mode frame analysis was conducted offline in MATLAB-Simulink using the sliding discrete Fourier transform (SDFT) algorithm [10]–[12]. The SDFT computes the complex Fourier coefficient value  $X_k$  of an  $N$ -point DFT for a single bin  $k$  for each input sample  $x$ . In our case, the input samples are grayscale pixel intensity values from the B-mode frame. As a window of length  $N$  increments across samples in time, each new DFT result is computed from the previous according to

$$X_k(n) = e^{j2\pi k/N} [X_k(n-1) + x(n) - x(n-N)], \quad (2)$$

where  $n$  is the time index and  $k$  is the frequency bin number. Since we are only interested in one bin, which is the bin that corresponds to the oscillation frequency of the flashing, the SDFT is significantly more computationally efficient than computing the entire fast Fourier transform (FFT), and also more efficient than the single-bin Goertzel filter (which was used in US-APA) [13]. The traditional SDFT based on Equation 2 can be implemented as an infinite impulse response filter; however, it is marginally stable because its pole resides on the z-domain's unit circle. Several alternative, stable SDFT networks have been proposed; one of the more accurate and computationally efficient networks is detailed in [10], requiring only eight real multiplies and nine real additions per input sample. Using the Simulink model in [12] (which was based on the SDFT network in [10]) as a framework, grayscale B-mode frames were fed into the

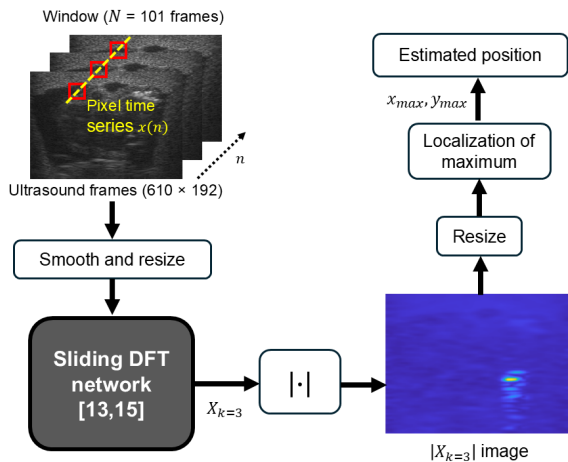


Fig. 3. SDFT-based algorithm pipeline.

model in sequence, where they were first smoothed to remove Gaussian noise, then resized to 25% of their original size to improve computation speed. Next, the frames were analyzed at the pixel level with the stable SDFT network using a window length of

$$N = \frac{3f_s}{f_{osc}} = 101,$$

where  $f_s$  is the frame rate of the ultrasound system ( $\sim 67$  Hz) and  $f_{osc}$  is the oscillation frequency (2 Hz). Hence,

$$k = N \frac{f_{osc}}{f_s} = 3.$$

The network outputted the value of  $X_{k=3}$  for all pixels in the (resized) frames at each time step, per window, which were then resized back to their original size. The position of the maximum value of  $|X_{k=3}|$  in each frame was taken to be the position of the dynamic CCR. The algorithm pipeline is shown in Figure 3.

## IV. RESULTS

This section describes the characterization of the dynamic CCR and quantifies the tracking error of the SDFT-based algorithm under different probe motion schemes. Tracking was accomplished with update rates of up to 120 Hz. Sample tracking videos can be found in the supplemental materials.

#### A. Characterization of the Dynamic CCR

Figures 4(a) and (b) demonstrate the effect of different  $B_{ext}$  on the dynamic CCR's opening angle  $\phi$  and brightness in ultrasound B-mode. Pixel intensities were measured using ImageJ software [14] by defining an elliptical region of interest that enclosed the bright region created by the dynamic CCR. The same region of interest was applied across all images. The mean pixel intensity for all pixels in the region of interest per field strength was calculated. The opening angle  $\phi$  was also measured in ImageJ.

As predicted,  $\phi$  increases with increasing field strength, which exposes more reflective surface area in the direction of the probe, increasing pixel brightness. The maximum opening angle achieved was  $76.4^\circ$  at 46 mT, which corresponded to a distance of 4.5 cm from the center of the permanent magnet to the center of the mock capsule. The experimental required opening field of 46 mT agreed well with the theoretical required field, which was also 46 mT. At field strengths greater than 46 mT, the gradient produced by the permanent magnet pulled the mock capsule towards it, making image acquisition unachievable.

#### B. Tracking with a Stationary Probe

Ultrasound B-mode frames were collected with a stationary probe. The ground truth position of the dynamic CCR was determined using visual inspection. Specifically, the ground truth was labeled using the faint outlines of the mock capsule boundary in the image to extrapolate the true position of the CCR. The Fourier spectrum of the ground truth position across all frames is shown in Figure 4(c), demonstrating that the peak oscillation frequency is at 2 Hz,

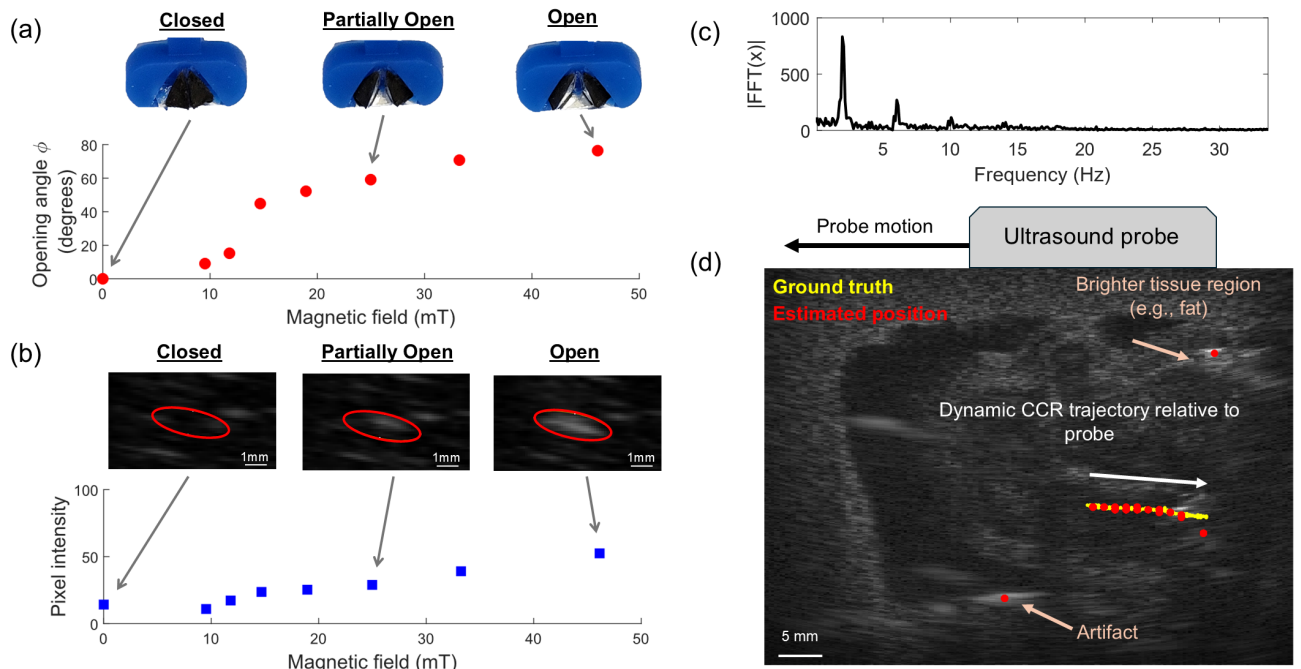


Fig. 4. (a) Opening angle  $\phi$  for each applied magnetic field strength. Images of dynamic CCR are shown for fields of 0 mT, 25 mT, and 46 mT. (b) Pixel intensities (mean) for each applied magnetic field strength. Dynamic CCR appearance in B-mode (region of interest labelled with red circle) is shown for fields of 0 mT, 25 mT, and 46 mT. (c) Frequency spectrum of a stationary dynamic CCR at ground truth position. (d) Tracked trajectory of stationary dynamic CCR relative to in-plane moving probe.

as expected, with minor peaks present at harmonics. Tracking error was calculated as the distance between the estimated centroid position of the dynamic CCR and the ground truth centroid position. The mean tracking error across all frames was 2.2 mm, which corresponds to 18% of the capsule's body length ( $n = 3650$  frames across 5 trials).

### C. Tracking with an In-Plane Moving Probe

For ultrasound B-frames collected with a probe moving linearly within the imaging plane, mean estimation error was 3.0 mm, which corresponds to 25% of the capsule's body length ( $n = 1503$  frames across 5 trials). Probe motion causes B-mode speckle motion that increases the frequency content of the background. Therefore, there is more background noise which occasionally is detected instead of the dynamic CCR. It can be seen in Figure 4(d) that incorrectly tracked background points tend to appear at areas of higher brightness, such as fatty tissue or image artifacts. Although not implemented in this work so as to evaluate the basic algorithm, these jumps in the estimated position can be minimized through temporal smoothing using a sliding median filter or a Kalman filter.

## V. DISCUSSION AND CONCLUSION

An important consideration for this device is its integration with a functioning robotic capsule. Integration may be particularly challenging for capsules that are magnetically actuated because the actuation of the dynamic CCR must not interfere with the actuation of the capsule itself. In this scenario, there may be up to three magnetic fields: the

steering field for locomotion, the tracking field for dynamic CCR actuation, and the activation field to initiate the capsule task (e.g., sampling, biopsy, drug delivery). One approach for dynamic CCR integration is to have the tracking field strength be lower than the activation field strength, so that tracking is possible without interference with task activation. Due to unique design differences, the activation of current capsules occurs within a large range of around 5–75mT [15]–[20]. The proposed dynamic CCR requires fields that may be suitable (25–46mT) for integration with existing capsules. For capsules that require steering, a potential approach could be to apply a rotating magnetic field, which produces a rotating torque on the dynamic CCR's net magnetic moment to roll the capsule about its long axis. Note that this would involve orienting the dynamic CCR so that its net moment aligns with the capsule's short axis (in this work the moment is aligned with the long axis). As the capsule rolls, the CCR will alternate between being exposed to and hidden from the ultrasound probe, producing a similar flashing pattern that can be tracked. The dynamic CCR's net magnetic field, however, can also be a limitation if it interferes with existing magnets in the capsule.

The size of the dynamic CCR is another limitation. Due to size constraints for ingestible endoscopic capsules, most existing capsules are unlikely to have extra space to accommodate the dynamic CCR at its current size ( $\sim 5$ mm). Therefore, proper integration of the dynamic CCR would require miniaturizing the device further, such as by using micro-fabrication techniques or machining. However, it should be noted that scaling down the CCR will increase

the attractive force between panels due to their reduced separation distance, as well as reduce the opening torque due to reduced panel magnetic moments, ultimately resulting in a larger required field for actuation. The size of the flashing pixel area will also be reduced, which may impact tracking accuracy. Investigation of the effect of reduced CCR size on tracking accuracy and required field will be a focus of future work. A final limitation is that the panel opening angle  $\phi$  was not able to reach the ideal  $90^\circ$ , likely due to a combination of friction between the panels and the cavity walls and a non-negligible stiffness from the hinge. Despite the imperfect CCR, the flashing in B-mode was still highly visible.

The SDFT tracking update rate (120 Hz) was greater than the ultrasound frame rate (67 Hz), meaning that tracking could theoretically be achieved in real-time with no reduction in frame rate. Although the SDFT permits real-time update rates, the real-time output of an  $N$ -point SDFT is a collective measure of the spectral content of  $N$  samples from the past. In this study, the window length was set to  $N = 101$  frames to capture three sinusoidal oscillations. Consequently, the true estimate of the DFT magnitude only occurs after  $N/f_s = 1.5s$ . However, the latency could be improved if oscillation frequency were increased, which would allow for a shorter required window. Higher oscillation frequencies would also enable higher probe speeds during tracking.

Future work will focus on dynamic CCR integration with a functioning robotic capsule to achieve locomotion and targeted sampling under real-time tracking. An important quality for clinical application, which will also be a focus of future work, is to achieve 3D localization by scanning the probe in the direction normal to the imaging plane. The current work was limited to in-plane tracking of the dynamic CCR, but out-of-plane tracking would enable detection of the presence and absence of the capsule. Dynamic CCR detection could be achieved by setting a threshold for  $|X_{k=3}|$ . Finally, it will also be important to evaluate capsule tracking using a curvilinear ultrasound probe at greater imaging depths along with simulated intraluminal gas to better replicate clinical abdominal imaging conditions. The fan-shaped beam produced by a curvilinear probe and increased imaging distance will likely weaken the CCR's retroreflection, and bright artifacts produced by gas may confound tracking.

#### ACKNOWLEDGMENT

The authors would like to thank Larissa Jin and Daniel Sieben for providing advice and experimental assistance.

#### REFERENCES

- [1] C. F. Keogh and P. L. Cooperberg, "Is It Real or Is It an Artifact," *Ultrasound Quarterly*, vol. 17, no. 4, pp. 201–210, 2001.
- [2] Q. Wang, K. F. Chan, K. Schweizer, X. Du, D. Jin, S. Chun, H. Yu, B. J. Nelson, and L. Zhang, "Ultrasound Doppler-guided real-time navigation of a magnetic microswarm for active endovascular delivery," *Science Advances*, vol. 7, p. eabe5914, 2021.
- [3] S. Pane, M. Zhang, V. Iacovacci, L. Zhang, and A. Menciassi, "Contrast-enhanced ultrasound tracking of helical propellers with acoustic phase analysis and comparison with color Doppler," *APL Bioengineering*, vol. 6, no. 3, 2022.
- [4] S. Pane, V. Iacovacci, E. Sinibaldi, and A. Menciassi, "Real-time imaging and tracking of microrobots in tissues using ultrasound phase analysis," *Applied Physics Letters*, vol. 118, no. 1, p. 014102, 2021.
- [5] S. Pane, V. Iacovacci, M. H. D. Ansari, and A. Menciassi, "Dynamic tracking of a magnetic micro-roller using ultrasound phase analysis," *Scientific Reports*, vol. 11, no. 1, p. 014102, 2021.
- [6] S. Pane, G. Faoro, E. Sinibaldi, V. Iacovacci, and A. Menciassi, "Ultrasound Acoustic Phase Analysis Enables Robotic Visual-Servoing of Magnetic Microrobots," *IEEE Transactions on Robotics*, vol. 38, no. 3, pp. 1571–1582, 2022.
- [7] G. Faoro, V. Iacovacci, and A. Menciassi, "Optical Flow and Acoustic Phase Analysis Comparison in Ultrasound-Based Microrobot Tracking," *IEEE Robotics and Automation Letters*, vol. 9, no. 2, pp. 1985–1992, 2024.
- [8] V. Grand-Perret, J. R. Jacquet, I. Leguerney, B. Benatsou, J. M. Grégoire, G. Willoquet, A. Bouakaz, N. Lassau, and S. Pitre-Champagnat, "A Novel Microflow Phantom Dedicated to Ultrasound Microvascular Measurements," *Ultrasonic Imaging*, vol. 40, no. 5, pp. 325–338, 2018.
- [9] D. W. Rickey, P. A. Picot, D. A. Christopher, and A. Fenster, "A wall-less vessel phantom for Doppler ultrasound studies," *Ultrasound in Medicine & Biology*, vol. 21, no. 9, pp. 1163–1176, 1995.
- [10] R. Lyons and C. Howard, "Improvements to the Sliding Discrete Fourier Transform Algorithm [Tips & Tricks]," *IEEE Signal Processing Magazine*, vol. 38, no. 4, pp. 119–127, 2021.
- [11] C. Q. Howard, "Application of Improved Sliding DFT Algorithm for Non-Integer  $k$ ," in *Acoustics 2021, Annual Conference of the Australian Acoustical Society*, Wollongong, New South Wales, Australia, 2022.
- [12] C. Howard, "Simulink model of Sliding DFT at exact analysis frequency," 2021. [Online]. Available: <https://www.mathworks.com/matlabcentral/fileexchange/101944-simulink-model-of-sliding-dft-at-exact-analysis-frequency>
- [13] P. Sysel and P. Rajmic, "Goertzel algorithm generalized to non-integer multiples of fundamental frequency," *Eurasip Journal on Advances in Signal Processing*, vol. 2012, no. 1, 2012.
- [14] C. A. Schneider, W. S. Rasband, and K. W. Eliceiri, "NIH Image to ImageJ: 25 years of image analysis," *Nature Methods*, vol. 9, pp. 671–675, 2012.
- [15] P. Shokrollahi, Y. P. Lai, S. Rash-Ahmadi, V. Stewart, M. Mohammadigheisar, L. A. Huber, N. Matsuura, A. E. Zavodni, J. Parkinson, and E. Diller, "Blindly Controlled Magnetically Actuated Capsule for Noninvasive Sampling of the Gastrointestinal Microbiome," *IEEE/ASME Transactions on Mechatronics*, vol. 26, no. 5, pp. 2616–2628, 2021.
- [16] J. Nam, Y. P. Lai, L. Gauthier, G. Jang, and E. Diller, "Resonance-based design of wireless magnetic capsule for effective sampling of microbiome in gastrointestinal tract," *Sensors and Actuators A: Physical*, vol. 342, 2022.
- [17] S. Park, H. Lee, D. I. Kim, H. Kee, and S. Park, "Active Multiple-Sampling Capsule for Gut Microbiome," *IEEE/ASME Transactions on Mechatronics*, vol. 27, no. 6, pp. 4384–4395, 2022.
- [18] M. Finocchiaro, C. Giosuè, G. Drago, F. Cibella, A. Menciassi, M. Sprovieri, and G. Ciuti, "Design of a magnetic actuation system for a microbiota-collection ingestible capsule," in *Proceedings - IEEE International Conference on Robotics and Automation*, vol. 2021-May. Institute of Electrical and Electronics Engineers Inc., 2021, pp. 6905–6911.
- [19] K. Esendag, M. E. McAlindon, D. Rus, S. Miyashita, and D. D. Damian, "A Chemical Reaction-Driven Untethered Volume Changing Robotic Capsule for Tissue Dilation," *IEEE Transactions on Medical Robotics and Bionics*, vol. 6, no. 4, pp. 1300–1308, 2024.
- [20] X. Dong, B. Xiao, H. Vu, H. Lin, and M. Sitti, "Millimeter-scale soft capsules for sampling liquids in fluid-filled confined spaces," *Science Advances*, vol. 10, no. 35, 2024.